

Characterization of Pore Wall Heterogeneity in Nanoporous Carbons Using Adsorption: the Slit Pore Model Revisited

Thanh X. Nguyen and Suresh K. Bhatia*

Division of Chemical Engineering, the University of Queensland, Brisbane, QLD 4072, Australia

Received: March 3, 2004; In Final Form: July 9, 2004

In this paper, we propose a new nonlocal density functional theory characterization procedure, the finite wall thickness model, for nanoporous carbons, whereby heterogeneity of pore size and pore walls in the carbon is probed simultaneously. We determine the pore size distributions and pore wall thickness distributions of several commercial activated carbons and coal chars, with good correspondence with X-ray diffraction. It is shown that the conventional infinite wall thickness approach overestimates the pore size slightly. Pore–pore correlation has been shown to have a negligible effect on prediction of pore size and pore wall thickness distributions for small molecules such as argon used in characterization. By utilizing the structural parameters (pore size and pore wall thickness distribution) in the generalized adsorption isotherm (GAI) we are able to predict adsorption uptake of supercritical gases in BPL and Norit R1 Extra carbons, in excellent agreement with experimental adsorption uptake data up to 60 MPa. The method offers a useful technique for probing features of the solid skeleton, hitherto studied by crystallographic methods.

1. Introduction

Porous carbons have long been used for gaseous and liquid phase adsorptive separations as well as storage of volatile compounds, because of their high surface area and strong adsorption forces arising from a high site density of close-packed sp^2 carbon atoms in a graphitic structure. The synthesis and manufacture of carbons with desired adsorptive properties requires reliable characterization of the internal structure of the carbon, which can be used for predicting adsorption equilibrium and kinetics from a mature understanding of the behavior of fluids in confined spaces. However, in practice the microstructure of porous carbon is complex and poorly understood due to its highly disordered nature. This leads to difficulty in accurately characterizing the pore morphology and topology even with modern visualization techniques such as high-resolution transmission electron microscopy (HRTEM) or by X-ray diffraction (XRD) and small-angle X-ray scattering. Consequently, the traditional indirect method of characterization in terms of an idealized structural model, based on analysis of gas adsorption data, is still the most commonly employed technique and provides a powerful complement to the above methods for interpreting the internal structures of porous carbons.

The most common idealization of the pore structure of carbons is that of a collection of independent slit pores having infinitely thick walls. Although disadvantages of the slit pore model are recognized,¹ it is widely used for characterization of activated carbons² because of its simplicity, which also permits the application of molecular level theories in describing confined fluid behavior. Some of the disadvantages, such as the exaggeration of short-range ordering, have been overcome by recently developed alternatives^{3–7} based on reverse Monte Carlo (RMC) simulation, whereby the carbon structure is reconstructed by fitting the radial distribution function of the carbon atoms determined by diffraction (e.g., XRD) techniques. However,

such models are computationally too demanding for routine use in characterization,² and the slit pore model remains the one most commonly used in structural characterization and analysis of adsorption behavior.

A complication inherent to carbons is the energetic heterogeneity arising from the presence of disorder at varying length scales, and in the case of slit pore characterization this heterogeneity is generally consigned to a single structural source represented by a pore size distribution. The latter is obtained by fitting gas adsorption data, using nonlocal density functional theory (NLDFT) to provide pore size dependent theoretical isotherms, while assuming infinitely thick pore walls.^{1,2,8–10} The approach, however, normally yields a systematic S-shaped deviation between fitted and experimental isotherms in the relative pressure range of 10^{-3} to 10^{-4} , but recent work has shown¹¹ that this deviation can be mitigated by assuming mixed pore walls, in which one wall is infinitely thick while the other has a single carbon layer. This suggests the existence of an additional structural heterogeneity in the form of pore wall heterogeneity in carbons, which needs to be considered in the slit pore model. Furthermore, the assumption regarding infinite pore wall thickness is also inconsistent with results from XRD and HRTEM,^{12,13} which reveal a high proportion of single-layer walls.

The inappropriateness of the infinitely thick wall assumption has recently been demonstrated in our own laboratory, based on a carbon mass balance on the pore walls, which yields a simple relation¹⁴

$$\gamma = \frac{2N_o}{\rho_c M_c S_g} = \frac{2630}{S_g} = \frac{0.1315}{\int_0^\infty [f_\mu(H)/H] dH} \quad (1)$$

between the mean number of graphene layers per pore wall, γ , and the surface area, S_g (m^2/g) or the pore volume distribution, $f(H)$, expressed in units of $\text{cm}^3/(\text{g}\text{\AA})$. Here N_o is the Avogadro number, ρ_c is the surface density of carbon atoms in a layer

* To whom correspondence may be addressed. E-mail: sureshb@cheque.uq.edu.au.

(38.17 nm⁻²), and M_c is atomic weight of carbon. Since most nanoporous carbons have surface areas in the range of 1200–2000 m²/g, it is evident that the pore walls can have only about 1–2 layers on average, suggesting that the infinitely thick wall assumption might be problematic. Indeed DFT calculations¹⁴ showed that the stronger adsorption potential associated with the latter assumption leads to overprediction of the adsorbed amount by as much as a factor of 2 at low pressures, where solid–fluid interactions dominate. This study has also shown that pore wall thickness has a significant impact on adsorption behavior such as the pore filling pressure and the adsorbed density profile. Further, for thin walls comprised of only 1–2 graphene layers, fluctuations are also of concern, prompting the concept of a pore wall thickness distribution in carbons.¹⁴ Such an additional heterogeneity would be also supported by recent results⁵ showing very different adsorbate–adsorbent potential energy distributions for a single nitrogen molecule at 77 K, in two saccharose-based carbons having virtually identical pore size distributions as determined from their structures reconstructed by RMC simulation.

Another problem is selection of a suitable probing gas and adsorption conditions for which predicted adsorption behavior is sensitive to the internal structure of the carbon. Adsorption of nitrogen and argon at 77 K has been commonly used to characterize porous carbons.^{11,15,16} However, Jiang et al.¹⁷ significantly overpredict methane adsorption on activated carbon and carbon fibers when using the pore size distribution (PSD) obtained from adsorption data of nitrogen at 77 K. Scaife et al.¹⁸ showed that use of the PSD obtained from the adsorption data of nitrogen and argon in AX21 carbon at 77 K leads to significant underestimation of adsorption uptake of carbon dioxide in the same carbon, which is attributed to the freezing of nitrogen and argon in the pore junctions or pores. Furthermore, these authors also showed that use of the PSD obtained from adsorption of carbon dioxide at 293 K predicts reasonably well argon and nitrogen adsorption up to 1 bar at the same temperature. However, Heuchel et al.¹⁹ fail to predict methane uptake in A35/4 carbon at 293 K when the PSD obtained from adsorption of carbon dioxide in the same carbon is used.

Numerous efforts^{19–25} for determination of the pore size distribution of porous carbons using high-pressure adsorption of supercritical methane have been made recently. This approach, while reducing the S-shaped deviation from experimental data due to the nonexistence of capillary condensation at supercritical conditions, normally gives a predominance of larger pores (>30 Å) in the pore size distribution,^{20–22} which is not observed in the PSD obtained from adsorption data at low temperature (77 or 87 K). Further, inaccuracy in prediction of the adsorption of carbon dioxide in A35/4 carbon at 293 K, using the PSD obtained from supercritical adsorption of methane, has been reported.¹⁹

In a more recent development,²⁶ we have introduced a new NLDFT-based slit pore characterization approach, in which heterogeneities of pore size and pore wall thickness are simultaneously considered. The latter is represented by the pore wall thickness distribution (PWTd), with mean number of layers in the pore walls, γ , directly related to the associated pore size distribution, $f(H)$, through eq 1. This equation provides a constraint on the PWTd, permitting solution of the otherwise difficult characterization problem of simultaneously determining this distribution as well as the PSD, $f(H)$, from adsorption data. In the work reported here we demonstrate application of the proposed technique to the determination of pore wall thickness and pore size distributions of various commercial activated

carbons, as well as coal chars prepared in our laboratory, and investigate the variation in internal structure of the coal char with degree of activation. Good correlation of features of the pore wall thickness distribution so obtained with those determined by X-ray diffraction is also shown, providing support for the technique. We also investigate the effect of interaction between fluid molecules in neighboring pores with thin walls having one or two carbon sheets. Further, we use the PSD obtained from interpretation of argon adsorption in BPL and Norit R1 Extra carbons at 87 K, using the new approach, to predict supercritical adsorption of argon, methane, and ethane, with good success.

2. Theoretical Modeling

2.1. Density Functional Theory. In this work, we use the Tarazona²⁷ NLDFT to calculate the single pore density profile $\rho(\mathbf{r})$ of the adsorbed phase. The density profile of adsorbate is obtained by minimizing the grand potential Ω at fixed temperature, chemical potential, and the pore volume (T, μ, V) in the presence of the spatially varying external field ϕ_{ext} , with

$$\Omega[\rho(\mathbf{r})] = F[\rho(\mathbf{r})] - \int d\mathbf{r} [\mu - \phi_{\text{ext}}] \quad (2)$$

The intrinsic Helmholtz free energy, $F[\rho(\mathbf{r})]$, is generally determined from a first-order expansion about a reference system of hard spheres of diameter σ_h , under a mean field approximation, leading to

$$F[\rho(\mathbf{r})] = F_h[\rho(\mathbf{r}); \sigma_h] + \frac{1}{2} \int d\mathbf{r} \rho(\mathbf{r}) \int d\mathbf{r}' \rho(\mathbf{r}') \phi_{\text{att}}(|\mathbf{r} - \mathbf{r}'|) \quad (3)$$

where F_h is the Helmholtz free energy of the hard sphere system and is given as

$$F_h[\rho(\mathbf{r}); \sigma_h] = kT \int d\mathbf{r} \rho(\mathbf{r}) [\ln(\Lambda^3 \rho(\mathbf{r})) - 1] + kT \int d\mathbf{r} \rho(\mathbf{r}) f_{\text{ex}}[\bar{\rho}(\mathbf{r}); \sigma_h] \quad (4)$$

Here $\Lambda = h/(2\pi mkT)^{1/2}$ is the thermal de Broglie wavelength and f_{ex} is the Helmholtz free energy functional per fluid particle, calculated from the Carnahan–Starling equation of state for hard spheres,²⁸ at a suitably weighted density, $\bar{\rho}(\mathbf{r})$, following

$$\bar{\rho}(\mathbf{r}) = \int d\mathbf{r}' \omega(|\mathbf{r} - \mathbf{r}'|, \bar{\rho}(\mathbf{r})) d\mathbf{r}' \quad (5)$$

where the weighting function, $\omega(|\mathbf{r} - \mathbf{r}'|, \bar{\rho}(\mathbf{r}))$, is as prescribed by the Tarazona formulation.²⁹ The attractive part of fluid–fluid potential, ϕ_{att} , is determined by the Weeks–Chandler–Andersen (WCA) separation³⁰ of the fluid–fluid interaction potential, as discussed below.

2.2. Potential Models. The interaction potential between fluid molecules is taken as the Lennard–Jones (LJ) 12–6 potential

$$\phi_{\text{ff}}(r) = 4\epsilon_{\text{ff}} \left[\left(\frac{\sigma_{\text{ff}}}{r} \right)^{12} - \left(\frac{\sigma_{\text{ff}}}{r} \right)^6 \right] \quad (6)$$

where r is interparticle distance, σ_{ff} is collision diameter, and ϵ_{ff} is well depth. Following the WCA separation,³⁰ the attractive part of this potential is represented as

$$\begin{aligned} \phi_{\text{att}}(|\mathbf{r} - \mathbf{r}'|) &= \phi_{\text{ff}}(|\mathbf{r} - \mathbf{r}'|) & |\mathbf{r} - \mathbf{r}'| > r_m \\ &= -\epsilon_{\text{ff}} & |\mathbf{r} - \mathbf{r}'| < r_m \end{aligned} \quad (7)$$

where $r_m = 2^{1/6}\sigma_{\text{ff}}$. The interaction potential, $\phi_{\text{wf}}(z)$, between a

carbon wall and an adsorbate molecule is represented by³¹

$$\phi_{\text{wf}}(z, n) = 2\pi\rho_c\sigma_{\text{cf}}^2 \in_{\text{cf}} \sum_{i=0}^{n-1} \left[\frac{2}{5} \left(\frac{\sigma_{\text{cf}}}{z + i\Delta} \right)^{10} - \left(\frac{\sigma_{\text{cf}}}{z + i\Delta} \right)^4 \right], \quad z > 0 \quad (8)$$

Here z is the (center to center) distance between the fluid molecule and the pore wall surface, n is the number of graphene layers in the pore wall, Δ is interlayer spacing, and ρ_c is the number of carbon atoms per unit area in a single graphene layer. Following Steele,³¹ the parameters $\Delta = 0.335$ nm and $\rho_c = 38.17$ atoms·nm⁻², corresponding to graphite, are used.

The asymmetric external potential profile, $\phi_{\text{ext}}(z, l, m)$, for a slit-shaped pore having pore size H is determined from superposition of the potentials of the opposing pore walls

$$\phi_{\text{ext}}(z, l, m) = \phi_{\text{wf}}(z, l) + \phi_{\text{wf}}(H - z, m) \quad (9)$$

where l and m are the arbitrary numbers of graphene layers in the two opposing walls.

2.3. Adsorption Model. We use the general adsorption isotherm (GAI), whereby excess adsorbed amount $\Gamma_{\text{ex}}(P)$ is given as

$$\Gamma_{\text{ex}}(P) = \int [\hat{\rho}(P, H_{\text{in}}) - \rho_b] f(H_{\text{in}}) dH_{\text{in}} \quad (10)$$

where $f(H_{\text{in}})$ is the pore size distribution of the adsorbent, $H_{\text{in}} = (H_{\text{cc}} - \sigma_c)$ is the geometrical pore width, H_{cc} is the physical pore width, σ_c is the effective diameter of the carbon atom, and ρ_b is the bulk density. $\hat{\rho}(P, H_{\text{in}})$ is the average density in a pore of width H_{in} at a given pressure P . Definition of the average density is dependent upon pore models.

For the conventional infinite wall thickness (IWT) model, in which adsorbent–adsorbate potential is represented by the 10–4–3 solid–fluid potential,³¹ the average density is defined as

$$\hat{\rho}(P, H_{\text{in}}) = \frac{1}{H_{\text{in}}} \int_0^{H_{\text{cc}}} \rho(P, H_{\text{in}}, z) dz \quad (11)$$

where $\rho(P, H_{\text{in}}, z)$ is the local density profile obtained from the NLDFT. For the finite wall thickness (FWT) model, in which the adsorbate–wall potential is represented by eq 8, the average density is defined as¹⁴

$$\hat{\rho}(P, H_{\text{in}}) = \sum_{m=1}^{\infty} p(m) \sum_{l=1}^{\infty} p(l) \frac{1}{H_{\text{in}}} \int_0^{H_{\text{cc}}} \rho_{lm}(P, H_{\text{in}}, z) dz \quad (12)$$

where $p(n)$ is a wall thickness probability distribution and $\rho_{lm}(P, H_{\text{in}}, z)$ is the local density profile in a pore of geometrical width H_{in} , with the left wall having l graphene layers and the right wall having m layers, obtained from the NLDFT. Here we assume that the thicknesses of the two opposing walls of a pore are uncorrelated and that the interaction potential between adsorbed molecules in the neighboring pores is insignificant in comparison to the fluid–solid potential energy, justified by the recent study from this laboratory¹⁴ showing the former to have negligible effect on the isotherm for small molecules such as nitrogen.

2.4. Simultaneous Determination of Pore Size and Pore Wall Thickness Distributions. Earlier attempts at characterization considering finite pore walls have been largely ad hoc, utilizing arbitrary assumptions regarding the thicknesses of the confining walls,^{11,32} for instance, that one wall is infinitely thick while the other has exactly one graphene layer.¹¹ Such assump-

tions have resulted in unrealistic surface areas and have therefore not led to a viable solution. Our use of the probability distribution $p(n)$ eliminates such arbitrary assumptions.

In practice, the interaction potential energy is insensitive to stacking number n for thick walls having five or more carbon layers. Consequently, we lump the combined probability for all the thick walls having five or more carbon layers into $p(4+)$. The pore wall thickness distribution, $\mathbf{p} = \{p(n); n = 1, 2, 3, 4, 4+\}$, and the pore size distribution, $f(H_{\text{in}})$, can then be solved simultaneously by minimizing the deviation, δ , between the theoretically estimated adsorbed quantity, Γ_{ex} , and the corresponding experimental quantity, $C \exp(P)$, where

$$\delta = \|\Gamma_{\text{ex}} - C_{\text{exp}}\|^2 \quad (13)$$

with Γ_{ex} given by eqs 10 and 12. Minimization of δ following eq 13 is subjected to the following constraints

$$\sum_{n=1}^{4+} p(n) = 1, \quad \sum_{n=1}^4 np(n) + 5p(4+) \leq \gamma \quad (14)$$

and the mean number of graphene sheets in a pore wall, γ , is given as

$$\gamma = \frac{2630(1 - w_a)}{S_g} \quad (15)$$

which is a modification of eq 1 to allow for the presence of mineral matter in the carbon. Here w_a is the mass fraction ash content in the carbon and S_g is surface area of the adsorbent given by

$$S_g = \int_0^{\infty} \frac{2}{H_{\text{in}}} f(H_{\text{in}}) dH_{\text{in}} \quad (16)$$

Minimization of δ subjected to the constraints in the eqs 14 and 15 is performed using a genetic algorithm,³³ coupled with Tikhonov regularization.³⁴ The L-curve technique³⁵ is used for determining the regularization parameter. In particular, we employ the PSD obtained using the above procedure as the guessed PSD, f_{guess} , with the infinitely thick wall model used to determine the smoothing parameter. The guessed pore wall thickness distribution, $\mathbf{p}_{\text{guess}}$, is then determined using eqs 15 and 16 together with an appropriate statistical distribution.³⁶ The solution space in the vicinity of the guessed solution ($f_{\text{guess}}, \mathbf{p}_{\text{guess}}$) can then be generated using the constraints given in eq 14. Subsequently the solution of the PSD and PWT is searched in this space. The final solution of the PSD and PWT is obtained after a few iterations of the above procedure using the genetic algorithm,³³ in which the guessed solution ($f_{\text{guess}}, \mathbf{p}_{\text{guess}}$) for the next iteration is taken from the result of the previous iteration.

3. Experimental Section

The above approach has been applied to data of argon adsorption at 87 K, for a variety of commercial carbons, and coal chars prepared in our laboratory. The former were BPL, F-400, and PCB carbons manufactured by Calgon Corp., RB-2, ROW-0.8, ROX-0.8, Norit R1 Extra (R1E), and Sorbonorit B4 (B4) carbons produced by Norit, and a synthetic polymer-based activated carbon fiber, ACF-15, supplied by American Kynol Inc. The chars comprised of a series of partially oxidized samples of a demineralized Australian Yarrabee coal char, whose structure was recently examined in our laboratory at

various levels of oxidation in air^{37,38} at 653 K. All the carbons were degassed at 300 °C overnight prior to argon adsorption. A Micromeritics ASAP 2010 volumetric adsorption analyzer was used to obtain argon adsorption data at 87 K. The ash content of each carbon was determined gravimetrically following direct combustion in air at 873 K in a Lindberg box furnace. X-ray diffraction patterns of the carbons were also obtained using Cu K α radiation ($\lambda = 0.15406$ nm).

4. Results and Discussion

In what follows we present the results of application of the above technique to the characterization of the various carbons and coal chars and the comparisons with the results using the infinite wall thickness model. For the theoretical single pore argon isotherms at 87 K, employed in the characterizations, we used the LJ potential parameters $\sigma_f = 0.3375$ nm, $\epsilon_f/k = 110.2$ K for argon, and $\sigma_{cf} = 0.3362$ nm, $\epsilon_{cf} = 58.02$ K for carbon.¹⁵ The pore wall thickness distributions determined using the new method are also used to estimate a parallelism factor, which is correlated with its counterpart determined from XRD. We also study the effect of pore–pore correlations and show that these are indeed negligible for argon adsorption. Finally we demonstrate the applicability of the new pore structure characterization to the prediction of isotherms of other gases, with superior performance compared to the traditional infinite wall thickness approach.

4.1. Characterization of Activated Carbons. Results of PSD and PWT of the eight commercialized activated carbons obtained from interpretation of argon adsorption using the current approach and the infinite wall thickness model, as well as examples of comparisons of experimental and fitted isotherms, are presented in Figures 1–4. Further, all characteristic parameters for the carbon samples are provided in Table 1. From this table it can be observed that surface area, S_g , of the carbons estimated from the proposed model is significantly higher than that obtained from the infinite wall thickness wall model. This results from overestimation of fluid–wall interaction potential in the latter case, which leads to a shift of fitted pore size distribution to slightly larger pore size, as seen in the insets of Figures 1 and 3. A shift in the pore size distribution to narrower pores has also been noted in an earlier study using arbitrarily sized pore walls,¹¹ with some reduction in the S-shaped deviation between fitted and experimental isotherms, prominent in isotherm fits based on the infinitely thick wall assumption, when the opposing walls differ in thickness. As seen in the insets of Figures 2 and 4 the S-shaped deviation in the isotherms is completely eliminated by the current approach. In the case of pore volume, the infinitely thick pore wall model underestimates the value by only a small amount, as seen in Table 1. This is due to the slightly lower density of the condensed argon in the pores with finite thickness walls that have a weaker potential field.

From Figure 1, an interesting feature observed for pore size distributions of BPL, F400, and PCB carbons, obtained from the current approach, is that the position of the first major peak in the PSD of BPL and F400, which are bituminous coal based, is quite similar while differing with that for PCB carbon, produced from a coconut source. It has been suggested that the pores represented by the first major peak can be created by removal of organic matter blocking them at early stage of the activation process, noted as a sharp increase in surface area and pore volume at low conversion.³⁸ Taken together with our results this would suggest that the first major peak in the PSD can be a source indicator of activated carbon. However, this needs to

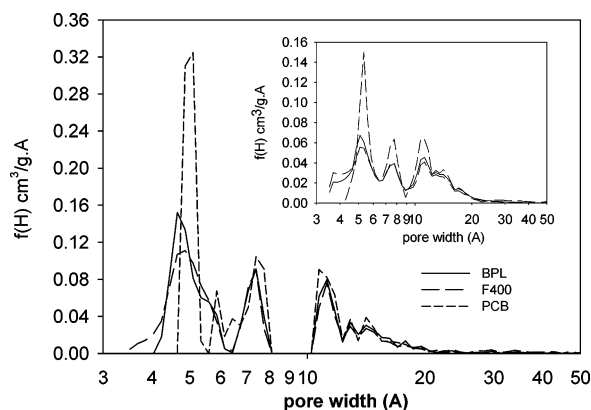


Figure 1. Pore size distribution of BPL, F400, and PCB activated carbon, from Calgon Corp., obtained by interpretation of argon adsorption at 87 K using the current approach. The inset depicts PSD using the conventional infinite wall thickness model.

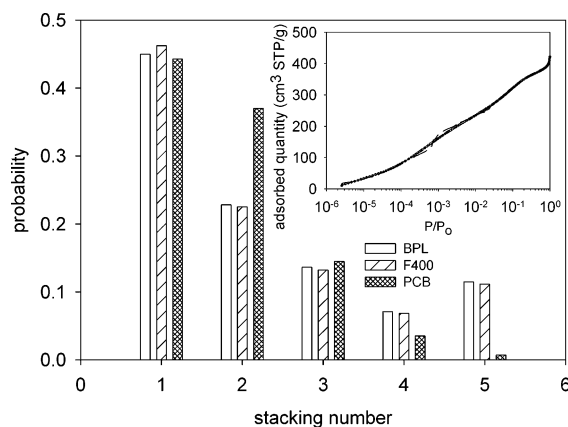


Figure 2. Pore wall thickness distribution of BPL, F400, and PCB activated carbons, obtained by interpretation of argon adsorption at 87 K using the current approach. The inset represents fitted and experimental argon adsorption isotherms for BPL carbon, illustrating the S-shaped deviation using the infinitely thick wall assumption, in the P/P_0 range lying between 10^{-4} and 10^{-3} . The solid line depicts the fitted isotherm obtained using the current approach, the dashed line depicts that using the conventional infinite wall thickness model, and the open circles are experimental measurements.

be confirmed with additional work on a variety of carbons. Interestingly, the positions of the first major peak of BPL, F400, and PCB carbons given by the infinite wall thickness model are indistinguishable, as seen in the insets in Figure 1, suggesting loss in resolution due to lumping all energetic heterogeneities into a single heterogeneity (pore size distribution).

Table 1 also lists the mean number of graphene sheets, γ , in a pore wall for each carbon, determined from the pore size distribution, based on eq 15 and the mineral matter content. The mean value of γ is found to be very low in general, and in the range of about 1.5–2, underscoring the inappropriateness of the assumption of infinitely thick walls. Besides highlighting the small wall thicknesses the pore size distributions also suggest that the carbon nanopores occur at discrete sizes or widths. This is evident from the sharp peaks in the distributions at discrete sizes from the application of the present approach, as opposed to the broad distribution peaks obtained from the infinite wall thickness approach. Furthermore, an average distance between the first three major peaks in the pore size distribution of the various carbons from the present approach is 3.23 Å, while the corresponding values from the infinite wall thickness model are almost constant at 3.04 Å. The former is quite close to the interlayer spacing of activated carbons of about 3.35 Å. This

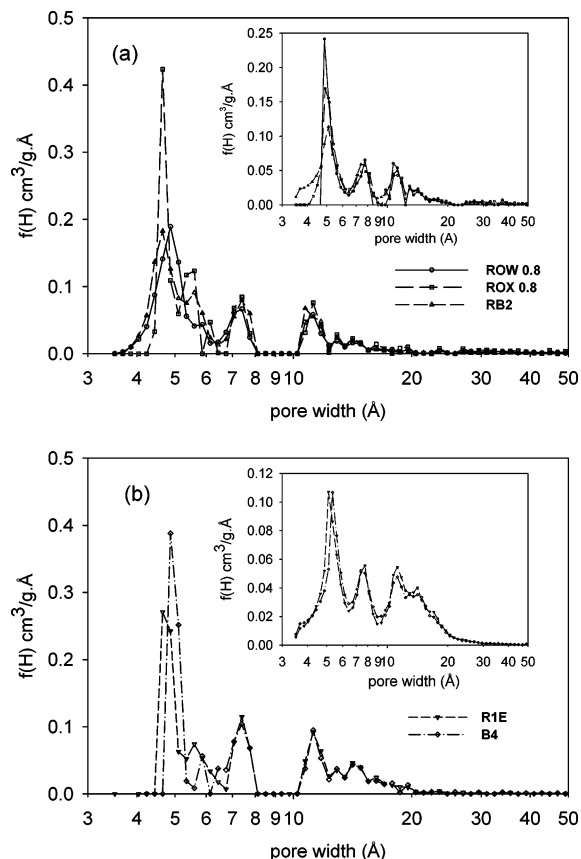


Figure 3. Pore size distribution of (a) Norit ROW0.8, ROX0.8, RB2, and (b) Norit R1 Extra and Sorbonorit B4 carbons, obtained by interpretation of argon adsorption at 87 K using the current approach. The inset shows the PSD using the conventional infinite wall thickness model.

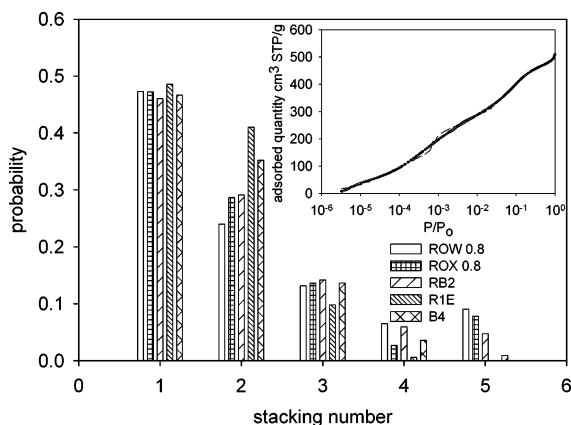


Figure 4. Pore wall thickness distribution of ROW0.8, ROX0.8, RB2, Norit R1 Extra, and Sorbonorit B4 carbons, obtained by interpretation of argon adsorption at 87 K using the current approach. The inset represents fitted and experimental argon adsorption isotherms for Norit R1 Extra, illustrating the S-shaped deviation using the assumption of infinitely wall thickness, in the P/P_0 range lying between 10^{-4} and 10^{-3} . The solid line depicts the fitted isotherm obtained using the current approach, the dashed line depicts that using the conventional infinite wall thickness model, and the open circles are the experimental measurements.

agreement may also suggest that the micropores are largely defects, such as clusters of missing planes, in crystallites. The effect of such defects on the adsorption field strength may be nontrivial in small pores represented by the first ($H_{in} \sim 4.44$ – 4.87 Å) and the second ($H_{in} \sim 7.34$ Å) major peaks, leading to poor resolution between these peaks, such as the right shoulder

TABLE 1: Comparison between Results Obtained for Activated Carbons Based on the Present Technique and Those Obtained Assuming Infinitely Thick Pore Walls

carbon	infinite wall thickness model		finite wall thickness model		γ
	S_g (m^2/g)	V_p (cm^3/g)	S_g (m^2/g)	V_p (cm^3/g)	
ACF-15	1446	0.52	1745	0.54	1.51
BPL	1023	0.51	1173	0.53	2.17
F-400	1012	0.55	1158	0.57	2.14
PCB	1178	0.55	1382	0.57	1.80
ROW 0.8	1034	0.59	1198	0.61	2.06
ROX 0.8	1161	0.65	1348	0.66	1.95
RB-2	1125	0.47	1294	0.49	1.94
R1E	1241	0.61	1461	0.64	1.62
B4	1206	0.61	1408	0.63	1.77

of the first major peak. On the other hand, such an effect is possibly minimal in larger pores represented by the third major peak ($H_{in} \sim 11.22$ Å), leading to a complete separation between the second and the third major peaks, with very low porosity between. This feature is also evident in the infinite pore wall thickness model, with low pore volume in the region of 0.9–1 nm. Finally, an increase in pore size after the third major peak results in less clearly resolved peaks due to weak sensitivity of the adsorption field strength at the large pore sizes.

While yielding the PSD and mean number of graphene sheets in the pore walls, the approach also provides the pore wall thickness distribution, $p(n)$, as shown in Figures 2 and 4 for the Calgon and Norit carbons, respectively. In these figures $p(5)$ represents the lumped probability for all the walls having five or more layers, given above as $p(4+)$. The large proportion of single-layer walls (45–60%) is evident from these figures and was found to be the case for all the carbons examined. While one may expect details of the pore wall thickness distribution to depend on the manufacturing process, the predominance of single-sheet walls appears to be a common feature for moderate and high surface area carbons. Further, it was also found that the pore wall thickness obtained from the isotherm fit could be well approximated by a generalized Poisson distribution³⁶ for most of the carbons except for ROX0.8, consistent with our earlier study.²⁶ On the other hand, for a carbon fiber the distribution fit well²⁶ to the limiting case of the Poisson distribution, corresponding to maximum randomness. Thus, the activated carbon fiber is expected to have a highly disordered structure in comparison to the activated carbons examined here. This will be further investigated in our work with a series of activated carbon fibers, to be reported in due course.

4.2. Characterization of Coal Chars. In this section, we utilize our approach for obtaining information on microstructure variations (pore size and pore wall thickness distributions) of coal chars with increasing degree of conversion. Figure 5 presents the variation in pore size distribution of the coal chars with increasing degree of conversion obtained from the current approach, and its inset depicts that obtained from the infinite wall thickness model. From Figure 5, it can be observed that the coal char with a low conversion of 7.46% has a rather uniform pore size, represented by the predominance of the first major peak, associated with a sharp increase in surface area compared to the original char which had much lower surface area.³⁸ In conjunction with XRD evidence of a significant fraction of disordered carbon, it has been surmised^{37,38} that such increase is due to the rapid gasification of disordered organic matter initially blocking the micropores. With an increase in conversion it is seen that there is a broadening of the PSD, with a gradual shift to larger pores. However, a significant shift of the position of the first major peak is seen only for the 80%

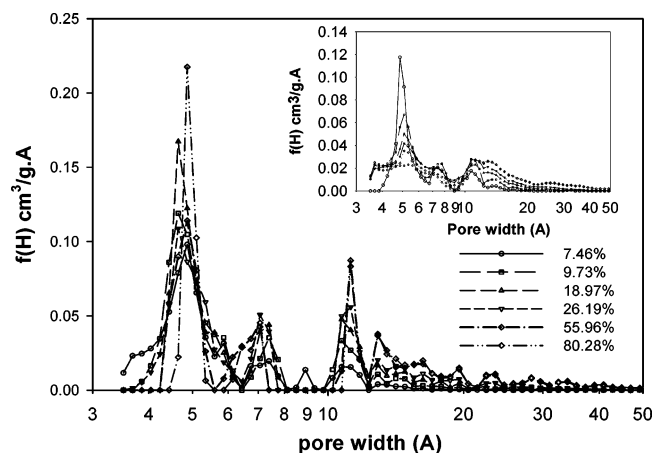


Figure 5. Pore size distribution of partially oxidized coal chars, derived from demineralized Australian Yarrabee coal char at different conversions, obtained by interpretation of argon adsorption at 87 K using the current approach. The inset depicts the PSD using the conventional infinite wall thickness model.

conversion char, for which the micropores appear to be larger. Following the earlier observation, based on the PSDs of the activated carbons, that micropores may correspond to clusters of missing planes in crystallites, the increase in micropore size at high conversion would indicate large crystallite strain and associated disorder at high conversion, as is to be expected. An interesting feature is noted here that the major peaks in PSD obtained from the current approach become sharper at higher conversions, indicating preferential etching of less ordered carbon layers.³⁹ In contrast, the results of the pore size distribution obtained by the infinite thickness model, as seen in the inset of the Figure 5, show that the major peaks become broader at higher conversions, a consequence of lumping all heterogeneities of porous carbons into nonuniformity of pore size as discussed below. Further, the peak separation is found to average about 3.19 Å using the current FWT model and about 2.94 Å for the IWT model. These are consistent with the earlier results for activated carbons and reinforce the conclusion that micropores are most likely defects, or clusters of missing planes, in crystallites. Another supporting feature is the low pore volume between the second and third peaks, in the region of 0.8–1 nm, consistent with the results for the carbons, except for the low-conversion char where some pore volume in this region is apparent. This may be related to defects in the parent char reducing the resolution in this region, but these appear to be eliminated on gasification.

Figure 6 presents results of the pore wall thickness distribution, with characteristic parameters given in Table 2 for the coal chars as determined by the current approach. From this figure, the coal char with conversion of 7.46% is seen to have a significant proportion of thick walls having more than five carbon sheets. An increase in conversion to 9.73% leads to a sharp decrease in proportion of thick walls having more than five carbon sheets, and an increase in corresponding proportion of thin wall types having one or two carbon sheets, while the proportion of the carbon wall types having three to four carbon layers is invariant. This indicates the predominance of the process of etching of carbon planes in small pores having thick walls to form larger pores having thinner walls, resulting in the growth in population of larger pores, as shown above. With an increase in conversion to 50%, it is interesting that the portion of thick wall types having five or more carbon sheets increases regularly, while a sharp decrease in the thin pore wall type having two carbon layers can be observed. Furthermore, the

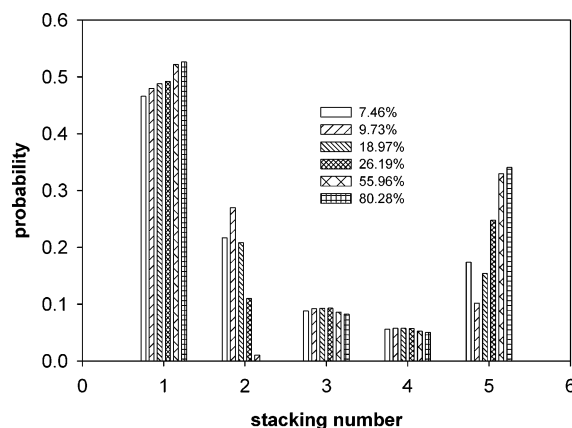


Figure 6. Pore wall thickness distribution of partially oxidized coal chars derived from demineralized Australian Yarrabee coal char, at different conversions, obtained by interpretation of argon adsorption at 87 K using the current approach.

TABLE 2: Comparison between Results Obtained for Coal Chars Based on the Present Technique and Those Obtained Assuming Infinitely Thick Pore Walls

conversion (%) ^a	infinite wall thickness wall		finite wall thickness model		γ
	S_p (m ² /g)	V_p (cm ³ /g)	S_p (m ² /g)	V_p (cm ³ /g)	
7.46	540	0.18	612	0.19	4.30
9.73	645	0.24	743	0.25	3.54
18.97	685	0.29	797	0.30	3.30
26.19	712	0.34	822	0.35	3.20
55.96	733	0.45	834	0.46	3.15
80.26	674	0.45	778	0.46	3.38

^a The first column represents degree of conversion in percentage, based on dry weight of the original demineralized coal char.

portion of the other pore wall types varies slightly. At a higher conversion of 80% the pore wall thickness distribution is essentially unchanged, though the proportion of two-layer walls drops drastically. These results are consistent with those reported by Sharma et al.,⁴⁰ who used HRTEM images to analyze variation in microstructure of a Pocahontas coal char. These authors found a significant increase in stacks having more than four carbon layers with increasing conversion (>42%), while most of the carbon loss comes from thin stacks having one to four carbon layers. Furthermore, Sharma et al.⁴⁰ also reported an increase in average stacking number for most of their investigated raw and demineralized coal chars with increasing conversion from 60% to 90%. A similar result is also observed for the coal chars studied here, at high conversion ranging from 56% to 80%.

Figure 6 also shows the broadening of the PWTd with conversion, simultaneously with narrowing of the PSD peaks shown in Figure 5, rationalizing the apparent broadening of the PSD peaks in the infinite wall thickness model where both heterogeneities are lumped together in the PSD. This demonstrates the pitfalls arising from such lumping in the IWT model. Interestingly, while the pore wall thickness distribution of the activated carbons, as shown earlier, can be well approximated by a generalized Poisson distribution, that of the coal char samples does not seem to conform well to this distribution, which may be related to the differences in carbon source and activation process and their combined effect on the PWTd.

Figure 7 illustrates a comparison of the experimental and fitted argon isotherms obtained from the present model and the infinitely thick wall model, for the various chars. It is seen that for the infinitely thick wall model the S-shaped deviation of the fitted isotherms from the experimental data becomes more

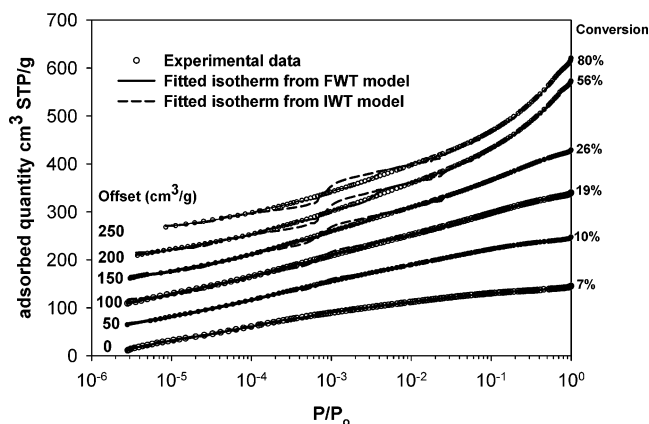


Figure 7. Fitted and experimental argon adsorption isotherms for the coal chars, illustrating the S-shaped deviation using the assumption of infinite wall thickness, in the P/P_0 range lying between 10^{-4} and 10^{-3} . The solid line depicts the fitted isotherm obtained using the current approach, the dashed line depicts that using the conventional infinite wall thickness model, and the open symbols are the experimental measurements of argon adsorption. For better resolution each curve is offset from the baseline by the amount given on its left.

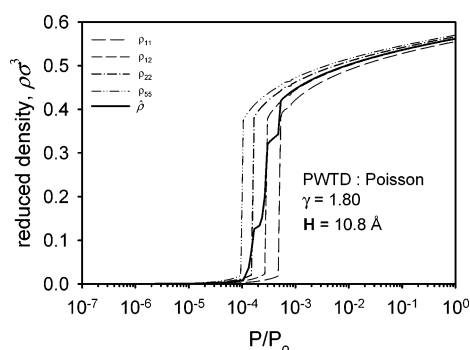


Figure 8. Argon adsorption isotherm at 87 K. ρ_{lm} is the local density in the pore type with the left wall having l carbon layers and the right wall having m carbon layers, and $\bar{\rho}$ is the average density calculated through eq 12.

pronounced with increasing conversion, while it is absent for the FWT model. This enhancement of the deviation is due to an increase in portion of larger pores at which capillary condensation occurs. For the infinitely thick wall model, whereby heterogeneity of pore walls in carbon is ignored, single pore isotherms in these larger pores have an abrupt change in density at condensation pressure leading to the S-shaped deviation from the experimental data.⁴¹ However, such abrupt change is removed in the isotherms obtained by the current approach through the pore wall heterogeneity, incorporated in eq 12, as seen in Figure 8 and also demonstrated in earlier work.¹⁴

4.3. Comparison with X-ray Diffraction. As an independent characterization of the solid phase the parallelism indicator, R , was determined from the (002) peak of the X-ray diffractograms as discussed above. This parameter has been used by Dahn et al.⁴² to estimate the fraction of graphene sheets that have no parallel neighbor. The (002) peak comes from constructive inference between X-rays scattered from parallel stacked graphene sheets. As the proportion of graphene layers with parallel neighbors increases, so will R . In terms of the probability distribution, $p(n)$, the fraction of graphene sheets in walls having more than one sheet is $[\gamma - p(1)]/\gamma$, which may be expected to have a direct correspondence with the X-ray parallelism indicator R . Parts a and b of Figure 9 depict, in turn, this relationship for the various activated carbons and coal chars investigated, illustrated in terms of a plot of R versus $[\gamma - p(1)]/\gamma$.

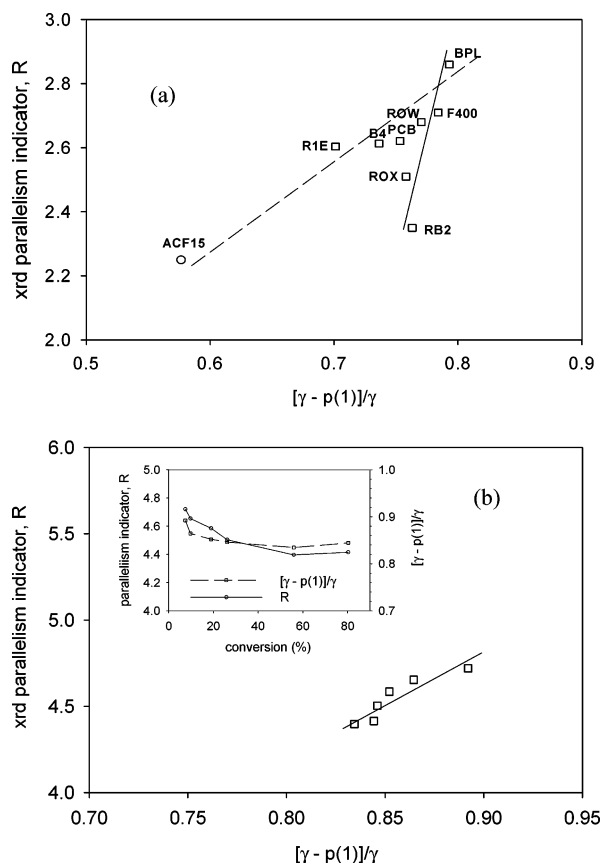


Figure 9. Correlation between the X-ray diffraction based parallelism indicator, R , and its counterpart, $[\gamma - p(1)]/\gamma$, determined by adsorption (a) for the activated carbons and (b) for coal chars at different conversions. In (b) the inset depicts the variation in the value of R and $[\gamma - p(1)]/\gamma$ with increasing conversion.

γ . In Figure 9a the open squares represent the data for the various coal-based activated carbons in Table 1, indicating a strong and nearly linear relationship between the two quantities for most of the investigated carbons. Given the somewhat diffuse nature of the (002) peak the parallelism indicator is not expected to be quantitatively precise. The good correlation between the adsorption and XRD-derived quantities, despite the approximate nature of R , is therefore representative of a strong correspondence between the two quantities for the carbons derived from a common precursor. In particular, the carbons of BPL, F400, RB2, and ROW0.8 and ROX 0.8 are known to be made from bituminous sources and indicate a good correlation between the adsorption and XRD-derived quantities for these carbons. Also shown in Figure 9a is the result for a synthetic polymer-derived activated carbon fiber, ACF-15, obtained earlier,²⁶ which deviates from this correlation along with Norit carbons R1 Extra and Sorbonorit R4, as well as Calgon PCB. While the source of R1Extra and B4 is unknown, that of Calgon PCB is coconut shell, and the different correlation offered by these materials, given by the dashed line in Figure 9a, may be related to the difference in their source from bituminous coal. This observation is supported by the results of Figure 9b and its inset, again showing a strong and nearly linear relationship between the adsorption and XRD quantities for the coal chars at various degrees of conversion prepared from the same demineralized Australian Yarrabee coal char.^{37,38} Thus, it is evident that a good correlation between the adsorption and XRD-derived quantities is observed for carbons prepared from the same source.

4.4. Effect of Pore–Pore Correlation on Adsorbent Characterization. An assumption associated with the above

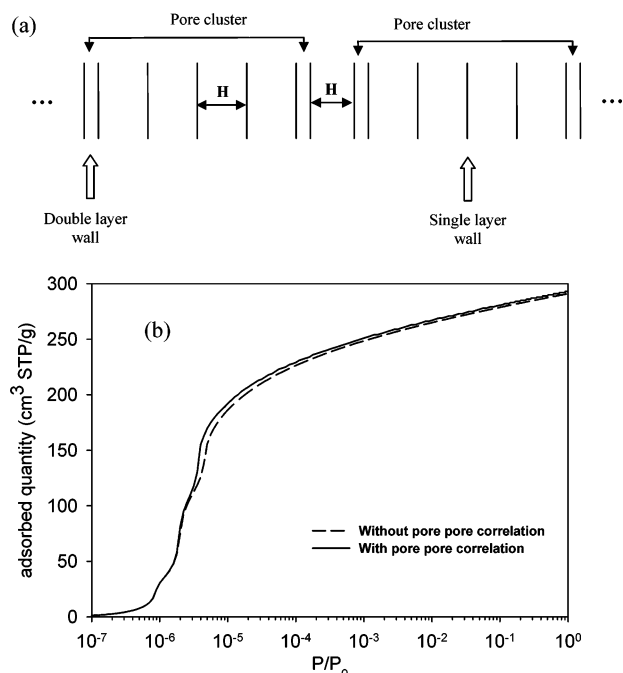


Figure 10. (a) Carbon model for investigating the effect of pore–pore correlation and (b) adsorption isotherms of argon at 87 K in the synthetic carbon with and without the effect of pore–pore correlation.

characterization technique is the insignificance of interpore interactions between the LJ fluid molecules adsorbed in neighboring pores. As noted in an earlier article,¹⁴ the effect of such pore–pore interaction is negligible for isotherms of small molecules such as nitrogen. In this section, we investigate the effect of the correlation on the argon adsorption isotherm at 87 K, as well as subsequent characterization of a synthetic carbonaceous adsorbent. For this we consider a synthetic model carbon having slit pores of uniform size with $H_{cc} = 7.8363$ Å, or $H_{in} = H_{cc} - \sigma_{cc} = 4.436$ Å. The pore topology is assumed to comprise a collection of identical pore clusters whose structure is illustrated in Figure 10a. The characteristic parameters of the model carbon consisting of surface area, S_g , pore volume, V_p , and mean wall thickness, γ , are presented in the first column of Table 3. The high surface area (~ 1900 m²/g) and the pore wall thickness distribution ($p(1) = 0.6$ and $p(2) = 0.4$) may cover a wide range of commercial carbons, based on the results presented above. From the carbon model, two kinds of synthetic argon adsorption isotherms for the carbon are generated. The first type, denoted ISO_1, is calculated from single pore isotherms without consideration of the pore–pore correlation, and the second type, denoted ISO_2, is determined while considering interpore interaction.

For calculation of the single pore isotherm in the case of interpore interaction, the external potential, $\phi_{ext}(z)$, is considered as a sum of the wall–fluid interaction potential, $\phi_{wf}(z)$, and the interaction potential due to adsorbate in the neighboring pores. The latter can be assumed to be equal to that caused only by adsorbed fluid in nearest neighbor pores, due to the fact that they are much weaker than the wall–fluid potential and are short-ranged. Thus, the external potential can be expressed in terms of the left side fluid–fluid potential, ϕ_{ff}^L , and right fluid–fluid potential, ϕ_{ff}^R , due to fluid in left and right neighboring pores, respectively, i.e.,

$$\phi_{ext}(z) = \phi_{wf}(z) + \phi_{wf}(H - z) + \phi_{ff}^L(z) + \phi_{ff}^R(z) \quad (17)$$

The potential due to interaction with a neighboring pore follows

$$\phi_{ff}^X(z) = \int \rho_X(z^X) \phi_{ff}^{10-4}(|z - z^X|) dz^X \quad (18)$$

with³¹

$$\phi_{ff}^{10-4} = 2\pi\epsilon_{ff}\sigma_{ff}^2 \left[\frac{2}{5} \left(\frac{\sigma_{ff}}{z} \right)^{10} - \left(\frac{\sigma_{ff}}{z} \right)^4 \right] \quad (19)$$

These two isotherms, presented in Figure 10b, are in turn used as experimental data to determine the internal structure of the synthetic carbon using our current approach and the infinite wall thickness model.

The results of the internal structure of the carbon obtained from interpretation of the two isotherms, ISO_1 and ISO_2, using the proposed approach and the infinitely thick wall model are given in Table 3 and Figure 11. From the results it can be seen that the current approach, neglecting interpore interaction, satisfactorily recovers all structural parameters of the carbon, even from the isotherm incorporating interpore interactions. The pore size distribution given by the current approach is sharp and matches with the input PSD, whereas the PSD obtained from the infinitely thick wall model is broader and has a shift to larger pore size. From Figure 11 and Table 3 it is evident that results from interpretation of the isotherms ISO_1 and ISO_2, using the finite wall thickness model, are nearly identical. Only a small deviation between the two results for the PWT is seen in Figure 11b. From the above results, one may conclude that pore–pore correlation has a negligible effect on calculated PSD and PWT obtained from interpretation of argon adsorption using the proposed model and that the independent pore NLDFT is satisfactory for small molecules such as argon.

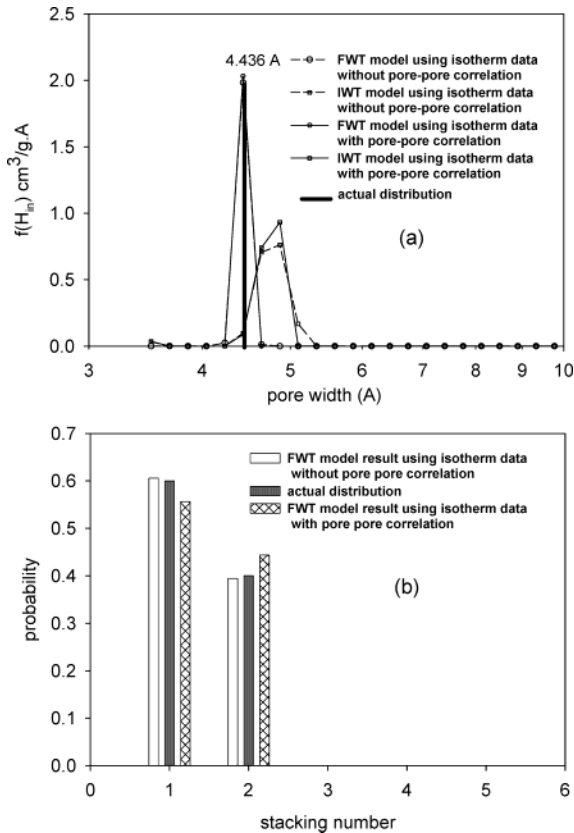
4.5. Application of the Model to Prediction of Adsorption of Supercritical Gases. An important test of the present characterization is its utility in predicting the equilibrium isotherms of other gases and the comparison of the performance with the traditional infinite wall thickness model. To this end, we used the structural parameters of BPL and Norit R1 Extra carbons, obtained from interpretation of argon adsorption at 87 K using the current approach and using the infinite wall thickness model, to predict adsorption of supercritical gases, argon, nitrogen, methane, and ethane, on these carbons. The adsorbates are modeled as single (LJ) site particles, with LJ parameters as given in Table 4. For argon, the Dombrowski et al.¹⁵ parameters used in characterization, determined by fitting vapor pressure data at low temperature, were not considered suitable for supercritical conditions. Consequently, for argon and methane the LJ parameters were taken to be the same as those used by Ustinov and Do,⁴³ obtained by fitting the NLDFT for the bulk fluid to the Bender equation of state at high pressures and 293 K. We also determined LJ parameters for ethane using the same approach. In the calculation, we used the values $\epsilon_c/k = 28.0$ K and $\sigma_{cc} = 0.34$ nm for carbon,³¹ with the cross parameters for the wall–fluid interaction potential determined through the Lorentz–Berthelot combining rules.

Figure 12a and its inset compare predictions and experimental data^{44,45} for the high-pressure adsorption of methane in BPL at 298 K. The solid line represents the predicted isotherm obtained using the PSD and PWT determined by the current FWT approach (Figures 1 and 2), while the dashed line represents that obtained from the use of the PSD given by the infinitely thick pore wall model. Further, open triangles depict experimental data in the low-pressure range up to 0.6 MPa taken from LeVan and Pigorini,⁴⁴ while circles depict data in the high-pressure range up to 60 MPa taken from Vidal et al.⁴⁵ The latter is measured using a precision dielectric method, which has been

TABLE 3: Comparison between Characteristic Parameters of the Synthetic Carbon Obtained from Finite Wall Thickness (FWT) and Infinite Wall Thickness (IWT) Models and Actual Values^a

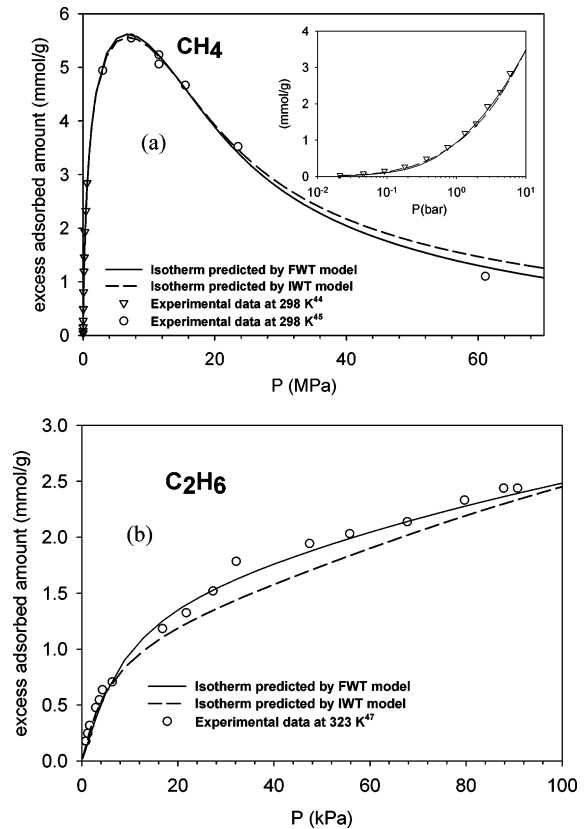
parameter	original value	FWT model		IWT model	
		ISO_1 input	ISO_2 input	ISO_1 input	ISO_2 input
S_g (m ² /g)	1879	1881	1893	1630	1658
V_p (cm ³ /g)	0.417	0.417	0.420	0.388	0.393
γ	1.400	1.398	1.389	na	na
$p(1)$	0.6	0.6057	0.5562	na	na
$p(2)$	0.4	0.3943	0.4438	na	na
$p(3)$	0	0	0	na	na
$p(4)$	0	0	0	na	na
$p(5)$	0	0	0	na	na

^a na implies that the parameter is not applicable to the IWT model.

**Figure 11.** Comparison of (a) pore size distribution of the synthetic carbon obtained using the current approach and the infinite wall thickness model and (b) the pore wall thickness distributions, obtained using isotherms with and without pore–pore correlation.**TABLE 4: Lennard-Jones Parameters for Fluid–Fluid Interaction of Argon, Methane, and Ethane at supercritical Condition**

gas	σ_{ff} (Å)	ϵ_{ff}/k_B (K)	source
Ar	3.2124	113.97	Ustinov et al. ⁴³
CH ₄	3.6177	146.91	Ustinov et al. ⁴³
C ₂ H ₆	4.045	223.35	present work

developed by Bose et al.⁴⁶ and then modified by Vidal et al.⁴⁵ The method obviates the need for a buoyancy correction, thereby overcoming a major drawback of the gravimetric technique at high pressure. From Figure 12a and its inset it is quite surprising to see that both approaches give excellent agreement with the experimental data up to about 60 MPa. Nevertheless, the infinite wall thickness model slightly overpredicts the experimental data at high pressure, due to its overprediction of the adsorbed phase density. While such overprediction also leads to the lower pore volume obtained from characterization under subcritical conditions, the latter is more than compensated for by the effect of

**Figure 12.** Predicted and experimental adsorption isotherms of methane and ethane in BPL carbon. The solid line depicts the predicted isotherm obtained from the finite wall thickness model and the dashed line represents that using the infinite wall thickness model. (a) Methane at 298 K. The inset presents the isotherms up to 0.6 MPa. The open triangles represent experimental data up to 0.6 MPa taken from LeVan and Pigorini⁴⁴ and the open circles represent data up to 60 MPa taken from Vidal et al.⁴⁵ (b) Ethane in BPL at 323 K. The open circles represent experimental data up to 1 bar taken from Russel and LeVan.⁴⁷

the density overprediction at the supercritical condition, where solid–fluid interaction is relatively more significant. Thus, it is clear that lumping of both heterogeneities into the PSD can only be adequate over a limited range of conditions.

Figure 12b illustrates the prediction of supercritical ethane adsorption in BPL carbon at 323 K. The experimental data are taken from Russel and LeVan.⁴⁷ In this case, use of the PSD and PWTB obtained from the finite wall thickness model provides excellent agreement with the experimental data, whereas use of the PSD obtained from the infinite wall thickness model underestimates the experimental data. This underestimation is most likely due to the relatively stronger fluid–fluid interaction for ethane as compared to the charac-

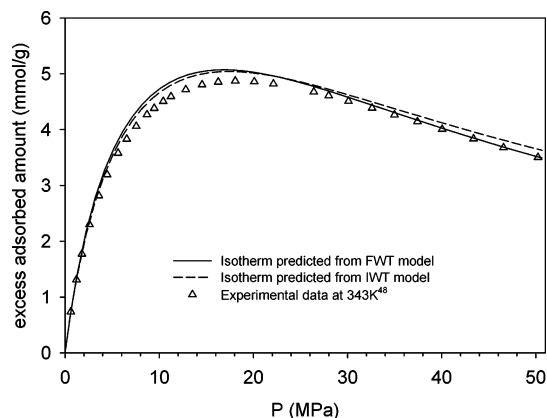


Figure 13. Predicted and experimental adsorption isotherms of argon in Norit R1 extra at 343 K. The solid line depicts the predicted isotherm obtained from the finite wall thickness model and the dashed line represents that using the infinite wall thickness model. Open triangles represent experimental data up to 50 MPa, taken from Herbst and Harting.⁴⁸

terization adsorptive argon, so that the density enhancement due to the stronger adsorption potential of the infinite wall thickness model is reduced in the case of ethane. This result clearly illustrates the problems in lumping both heterogeneities into the PSD.

Figure 13 presents the prediction of argon adsorption in Norit R1 Extra at 343 K. The experimental data of supercritical argon adsorption in Norit R1 at 343 K, obtained by thermogravimetry, are taken from Herbst and Harting.⁴⁸ As in the case of methane on BPL carbon, the predictions based on the current FWT model characterization agree with the data very well over the whole range from low to high pressure. However, the infinite wall thickness model again overpredicts at high pressure.

Thus, it is evident that the use of structural parameters of porous carbon obtained from interpretation of argon adsorption at 87 K enables one to predict correctly adsorption behavior of argon itself and of other species at supercritical conditions, providing that LJ parameters are determined properly. It is also evident that the use of PWTD and PSD simultaneously, as determined by the current approach, provides more accurate prediction of adsorption behavior than only PSD as characterized by the infinite wall thickness model, especially for large and strongly adsorbed species such as ethane. Furthermore, the successful use of cross LJ parameters, calculated from the Steele³¹ parameters for carbon and fluid LJ parameters obtained from fitting bulk fluid equilibrium through Lorentz–Berthelot combining rules, to predict supercritical adsorption, implies a reliable way to determine the cross terms for predicting supercritical adsorption of simple gases.

The success in prediction of adsorption of other species, based on the new FWT model, suggests that argon is a suitable choice of probing gas for the adsorption characterization. Its features of being spherical and small as well as nonpolar enable it to penetrate narrow pores, permitting more accurate characterization. Furthermore, the stronger adsorption of argon at its boiling point compared to that at supercritical conditions permits a more reliable determination of the carbon wall structure at the former condition. We hope to apply our approach to activated carbon fibers and other carbon materials in work to be reported in due course and thereby also obtain further supporting evidence for the technique. Nevertheless, despite its success it should be noted that the current approach, while distinguishing between pore size and pore wall thickness heterogeneities, does not capture chemical heterogeneities arising from functional groups attached

to the carbon surface at edge sites of crystallites. While apparently not important in the cases investigated here, the consideration of additional types of heterogeneities may be necessary in other carbon types.

5. Conclusions

In summary, the above results demonstrate that adsorption can be reliably used to probe the physical structure of the solid phase in carbons, conventionally studied by X-ray diffraction. In particular, consideration of the pore wall thickness distribution as a heterogeneity¹⁴ in addition to the pore size distribution permits improved fits of the low-temperature isotherms used in characterization, while revealing important information of the structure that correlates well with XRD results. The good correspondence with XRD, combined with the sharp PSD peaks, suggests that the narrow micropores are defects within the same crystallite, most likely arising from missing portions of neighboring graphene sheets. Nevertheless, some influence of inter-crystalline pore space, particularly in the larger pores beyond about 1 nm may be expected.

Pore–pore correlation, which is ignored in the current approach, has a negligible effect on results of pore size and pore wall thickness distributions. The use of structural parameters of porous carbon obtained from interpretation of the argon adsorption isotherm at 87 K, using the proposed model or the infinitely thick model, enables one to predict adsorption of small molecules such as methane and argon. However, the IWT approach may be less satisfactory and inadequate, particularly for larger and more strongly adsorbed molecules such as ethane. Thus, it is now clear that fitting a set of argon adsorption data at 87 K in porous carbon enables one to successfully predict adsorption of different supercritical gases in the same carbon, using the current FWT approach. This may enable one to better understand internal structural characteristics of porous carbon such as pore network connectivity,^{22,25} as well as the effect of the structure on processes of adsorption equilibrium and kinetics.

Acknowledgment. Financial support of this research by the Australian Research Council through the Discovery Grants scheme is gratefully acknowledged.

References and Notes

- (1) Lastoskie, C.; Gubbins, K. E.; Quirke, N. *Phys. Chem.* **1993**, *97*, 4786.
- (2) Bandosz, T. J.; Biggs, M. J.; Gubbins, K. E.; Hattori, Y.; Liyama, T.; Kaneko, K.; Pikunic, J.; Thomson, K. T. *Molecular Models of Porous Carbons*. In *Chemistry and Physics of Carbon*; Dekker: New York, 2003; Vol. 28; p 41.
- (3) O'Malley, B.; Snook, I.; McCulloch, D. *Phys. Rev. B* **1998**, *57*, 14148.
- (4) Opletal, G.; Petersen, T.; O'Malley, B.; Snook, I.; McCulloch, D. G.; Marks, N. A.; Yarovsky, I. *Mol. Simul.* **2002**, *28*, 927.
- (5) Pikunic, J.; Clinard, C.; Cohaut, N.; Gubbins, K. E.; Guet, J.-M.; Pellenq, R. J.-M.; Rannou, I.; Rouzaud, J.-N. *Langmuir* **2003**, *19*, 8565.
- (6) Petersen, T.; Yarovsky, I.; Snook, I.; McCulloch, D. G.; Opletal, G. *Carbon* **2003**, *41*, 2403.
- (7) Lastoskie, C. M.; Gubbins, K. E. *Characterization of Porous Materials Using Molecular Theory and Simulation*. In *Molecular Modeling and Theory in Chemical Engineering*; Chakraborty, A., Ed.; Academic Press: 2001; p 493.
- (8) Seaton, N. A.; Walton, J. P. R. P.; Quirke, N. *Carbon* **1989**, *27*, 853.
- (9) Vishnyakov, A.; Ravikovitch, P. I.; Neimark, A. V. *Langmuir* **1999**, *15*, 8736.
- (10) Bhatia, S. K. *Langmuir* **1998**, *14*, 6231.
- (11) Ravikovitch, P. I.; Jagiello, J.; Tolles, D.; Neimark, A. V. Improved DFT Methods for Micropore Characterization of Activated Carbons: Role of Pore Wall Heterogeneity, Presented at the American Carbon Society Carbon 2001 Conference, Lexington, KY, July 14–19, 2001.
- (12) Sharma, A.; Kyotani, T.; Tomita, A. *Fuel* **1999**, *78*, 1203.

- (13) Sharma, A.; Kyotani, T.; Tomita, A. *Carbon* **2000**, 38, 1977.
- (14) Bhatia, S. K. *Langmuir* **2002**, 18, 6845.
- (15) Dombrowski, R. J.; Hyduke, D. R.; Lastoskie, C. M. *Langmuir* **2000**, 16, 5041.
- (16) Ravikovitch, P. I.; Vishnyakov, A.; Russo, R.; Neimark, A. V. *Langmuir* **2000**, 16, 2311.
- (17) Jiang, S.; Zollweg, J. A.; Gubbins, K. E. *J. Phys. Chem.* **1994**, 98, 5709.
- (18) Scaife, S.; Kluson, P.; Quirke, N. *J. Phys. Chem. B* **2000**, 104, 313.
- (19) Heuchel, M.; Davies, G. M.; Buss, E.; Seaton, N. A. *Langmuir* **1999**, 15, 8695.
- (20) Gusev, V. Y.; O'Brien, J. A. *Langmuir* **1997**, 13, 2815.
- (21) Gusev, V. Y.; O'Brien, J. A. *Langmuir* **1997**, 13, 2822.
- (22) Davies, G. M.; Seaton, N. A. *Langmuir* **1999**, 15, 6263.
- (23) Davies, G. M.; Seaton, N. A. *AIChE J.* **2000**, 46, 1753.
- (24) Davies, G. M.; Seaton, N. A.; Vassiliadis, V. S. *Langmuir* **1999**, 15, 8235.
- (25) Lopez-Ramon, M. V.; Jagiello, J.; Bandosz, T. J.; Seaton, N. A. *Langmuir* **1997**, 13, 4445.
- (26) Nguyen, T. X.; Bhatia, S. K. *Langmuir* **2004**, 20, 3532.
- (27) Tarazona, P. *Phys. Rev. A* **1985**, 31, 2672; **1985**, 32, 3148.
- (28) Carnahan, N. F.; Starling, K. E. *J. Chem. Phys.* **1969**, 51, 635.
- (29) Tarazona, P.; Marini, B. M. U.; Evans, R. *Mol. Phys.* **1987**, 60, 573.
- (30) Weeks, J. D.; Chandler, D.; Andersen, H. C. *J. Chem. Phys.* **1971**, 54, 5237.
- (31) Steele, W. A. *Surf. Sci.* **1973**, 36, 317.
- (32) McEnaney, B.; Mays, T. J.; Chen, X. *Fuel* **1998**, 77, 557.
- (33) Zbigniew, M. *Genetic Algorithms + Data Structures = Evolution Programs*, 3rd ed.; Springer-Verlag: New York, Berlin, 1996.
- (34) Tikhonov, A. N. *Dokl. Akad. Nauk SSSR* **1963**, 49.
- (35) Hansen, P. C. *BIT* **1990**, 30, 658.
- (36) Consul, P. C. *Generalized Poisson Distributions: Properties and Applications*; Marcel Dekker: New York, 1989.
- (37) Feng, B.; Bhatia, S. K. *Energy Fuels* **2003**, 17, 744.
- (38) Feng, B.; Bhatia, S. K.; Barry, J. C. *Carbon* **2002**, 40, 481.
- (39) Sharma, A.; Kadooka, H.; Kyotani, T.; Tomita, A. *Energy Fuels* **2002**, 16, 54.
- (40) Sharma, A.; Kyotani, T.; Tomita, A. *Fuel* **1999**, 78, 1203.
- (41) Olivier, J. P. *Carbon* **1998**, 36, 1469.
- (42) Dahn, J. R.; Xing, W.; Gao, Y. *Carbon* **1997**, 35, 825.
- (43) Ustinov, E. A.; Do, D. D. *Langmuir* **2003**, 19, 8349.
- (44) LeVan, M. D.; Pigorini, G. Group-Contribution Theory for Adsorption of Gases and Vapors on Solid Surfaces. In *Foundations of Molecular Modeling and Simulation*; Keystone: Colorado, 1997.
- (45) Vidal, D.; Malbrunot, L.; Guengant, L.; Vermesse, J. *Rev. Sci. Instrum.* **1990**, 61, 1314.
- (46) Bose, T. K.; Chahine, R.; Marchildon, L.; St-Arnaud, J. M. *Rev. Sci. Instrum.* **1987**, 58, 2279.
- (47) Russell, B. P.; LeVan, M. D. *Ind. Eng. Chem. Res.* **1997**, 36, 2380.
- (48) Herbst, A.; Harting, P. *Adsorption* **2002**, 8, 111.